

UC Irvine

UC Irvine Previously Published Works

Title

In-Situ HF Forming Agents for Sustainable Manufacturing of Iron-Based Oxygen Reduction Reaction Electrocatalysis Synthesized Through Sacrificial Support Method.

Permalink

<https://escholarship.org/uc/item/3ks5423j>

Journal

Annali di Chimica, 18(3)

Authors

Mostoni, Silvia

Mirizzi, Lorenzo

Frigerio, Alessandra

et al.

Publication Date

2025-02-01

DOI

10.1002/cssc.202401185

Peer reviewed

In-Situ HF Forming Agents for Sustainable Manufacturing of Iron-Based Oxygen Reduction Reaction Electrocatalysis Synthesized Through Sacrificial Support Method

Silvia Mostoni⁺,^[a] Lorenzo Mirizzi⁺,^[a] Alessandra Frigerio⁺,^[a] Giovanni Zuccante,^[a, b] Chiara Ferrara,^[a] Mohsin Muhyuddin,^[a] Massimiliano D'Arienzo,^[a] Sara Fernanda Orsini,^[a] Roberto Scotti,^[a] Alessio Cosenza,^[c] Plamen Atanasov,^[c] and Carlo Santoro^{*,[a]}

Fe–N_x–Cs being suitable to replace scarce and overpriced platinum group metals (PGMs) for cathodic oxygen reduction reaction (ORR) are gaining significant importance in the fuel cell arena. Although the typical sacrificial support method (SSM) ensures the superior electrocatalytic activity of derived Fe–N_x–C, removing silica hard templates always remains a great challenge due to the hazardous use of highly toxic and not environmentally friendly hydrofluoric acid. Herein, strategic insight was given to modified SSM by exploiting the in-situ formation of HF, deriving from the decomposition of NH₄HF₂ and NaF, to dissolve silica templates, thus avoiding the direct use of HF. First, the suitable molar ratio between the etching

agent and the silica was analyzed, revealing that NH₄HF₂ efficiently dissolved silica even in a stoichiometric amount, whereas an excess of NaF was required. However, both etching agents exhibited conformal removal of silica while dispersed active moieties within the highly porous architecture of derived electrocatalysts were left behind. Moreover, NH₄HF₂-washed counterparts demonstrated relatively higher performance both in acidic and alkaline media. Notably, with NH₄HF₂-washed Fe–N_x–C electrocatalyst, a remarkable onset potential of 970 mV (vs RHE) was achieved with nearly tetra-electronic ORR as the peroxide yield remained less than 10% in the alkaline medium.

Introduction

The Hydrogen Economy presents a paramount technology of Fuel Cells (FCs) having the capability to sustainably convert chemical energy into green electrical energy without environmental impacts. The demand for FCs covers a broad spectrum of applications, ranging from domestic to industrial and even automotive sectors. For these scopes, low temperature (T) FCs are preferred to high T FCs because they are more prone to operate with intermittent loading.

The most mature low T FCs are the proton exchange membrane FCs (PEMFCs) that efficiently transform hydrogen into electricity. PEMFCs rely on electrocatalysts based on platinum supported over carbon (Pt/C) on both anode and cathode electrodes.^[1–4] On the anode, hydrogen is oxidized in

the so-called hydrogen oxidation reaction (HOR) while on the cathode, oxygen is reduced in the well-known oxygen reduction reaction (ORR). In PEMFCs, the ORR is sluggish, and therefore, higher Pt/C loading is needed to improve the kinetics and restrict the formation of intermediates while ensuring complete oxygen electro-reduction.^[5–7] Many improvements have been made in this sense by reducing the Pt/C loading,^[8–12] improving the electrocatalyst layer interface,^[13,14] enhancing the electrocatalyst utilization,^[15–17] and so on.^[18–20] It was also tried to substitute Pt/C with first-row transition metals (TMs) in the form of TM–N_x–C electrocatalysts.^[21–23] Despite this strategy being the most promising one, many issues are faced by this class of electrocatalysts while operating in acid media as recently summarized in a comprehensive review.^[24]

In the past 10–15 years, with the development of efficient anion exchange membrane (AEM), the interest and investments in AEMFCs have grown exponentially.^[25–27] In an alkaline environment, TM–N_x–C electrocatalysts can efficiently substitute Pt/C and therefore much attention has been devoted to this topic. Such electrocatalysts are based on TM–N_x–C with x = 2,3,4 and TM = Fe, Cu, Co, Mn, Ni, etc. integrated into a graphitic-like structure.^[28–33] These active sites are responsible for a direct 4e[−] transfer mechanism or for the reduction of the intermediate to the final product.^[34–36] In general, concerning ORR in alkaline media, it was shown that Fe is the most promising electrocatalyst mainly due to its suitable interaction with oxygen.^[37–39] Other active sites can be present on the carbon backbone, such as TM oxides, carbides and/or metallic nanoparticles.^[40,41] Importantly, also nitrogen moieties play an active role in ORR and in general it can be implied that they are

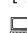
[a] Department of Materials Science, University of Milano-Bicocca U5, Milano, Italy


[b] Department of Industrial Engineering, University of Padova, Padova, Italy

[c] Department of Chemical and Biomolecular Engineering, University of California, Irvine, CA, United States

Correspondence: Carlo Santoro, Department of Materials Science, University of Milano-Bicocca U5, Via Roberto Cozzi 55, 20125, Milano, Italy. Email: carlo.santoro@unimib.it

[†] The three authors have contributed equally to the work.

 Supporting information for this article is available on the WWW under <https://doi.org/10.1002/cssc.202401185>

 © 2024 The Authors. ChemSusChem published by Wiley-VCH GmbH. This is an open access article under the terms of the Creative Commons Attribution License, which permits use, distribution and reproduction in any medium, provided the original work is properly cited.

responsible for reducing oxygen through a $2e^-$ transfer mechanism producing the undesired intermediate, $H_2O^- + OH^-$.^[40,42] Pyridinic nitrogen instead has been shown to be active toward the reduction of the intermediate in the final product, OH^- .^[43]

Different strategies are presented in the literature for synthesizing these electrocatalysts^[41] but, in general, four routes are the most explored and are here briefly presented. The first one uses TM containing azamacrocycles (e.g. phthalocyanine^[44–48] and porphyrins^[21,49–51]) as precursors that are mixed with a high surface area carbon support and are subjected to pyrolytic processes at different temperatures and different atmospheres.

In another synthetic route, porphyrins or other azamacrocycles can be used successfully as building blocks to create a covalent framework aerogel possessing high surface area and high active site density.^[52–55] The covalent framework is subject to supercritical CO_2 drying and then the aerogel is subject to pyrolysis at a controlled temperature and atmosphere to gain graphitization without losing its intrinsic high porosity.

Another route is based on the utilization of a covalent organic framework (COF) containing TM or metal-organic framework (MOF). In these cases, COF or MOF are prepared and are subject to pyrolysis processes to enhance graphitization while maintaining the morphological structure and preserving the desired TM– N_x –C active sites.^[56–61]

The fourth synthetic method considers the mixing of a nitrogen-rich organic precursor, a metal salt and a templating agent. Soft^[62–65] and hard^[66–68] templating are used with the first one being removed during pyrolysis, while the second one after the pyrolytic process. Hard templating is preferred because it helps within the graphitization process and creates a well-structured porosity.^[69–71] In this context, many nitrogen-rich organic precursors have been explored along with several metal salt precursors.^[72–74] Hard templating using silica with different sizes and morphologies has been also studied, leading to efficient ORR electrocatalysts.^[75] The synthetic route known as the sacrificial support method (SSM) relies on the pyrolytic process in a neutral and/or slightly reducing atmosphere at a temperature above 800 °C, where graphitic carbon formation is enhanced.^[76] The removal of the hard templating agent occurs afterward with the support of HF that etch out the silica and create a defined porosity and the pore size distribution depends on the silica size. After silica removal, the ORR electrocatalyst is subjected to a second pyrolysis in a reducing atmosphere.^[77] The last synthetic route is also the one that fabricates ORR electrocatalysts at a commercial scale through the company Pajarito Powder.^[69,78]

While this process is scalable and the ORR electrocatalysts synthesized are among the most efficient ever developed, the biggest bottleneck of the process lies in the utilization of HF, which is difficult to handle and its waste raises remarkable environmental concerns. Recently, the etching of silica was removed from the process by introducing polytetrafluoroethylene (PTFE) within the mixture (N-rich organic molecules, metal salt, silica templating) that allowed to obtain a defined porosity and efficient ORR^[79] and CO_2 reduction reaction

electrocatalyst.^[68] This innovative, smart and efficient methodology, prompted us to propose an alternative strategy to remove silica without using HF directly but by exploiting in-situ forming HF agents such as NH_4HF_2 and NaF. In this way, the direct utilization of HF is avoided, reducing the risk of handling a hazardous acid, and leading to an easier and safer synthetic route to fabricate efficient ORR electrocatalysts. The in-situ formation of HF enables the safer and minimal use of strong acids, while also facilitating the safe disposal of residues. In this framework, we here propose the design and development of a hard templating strategy for the production of Fe– N_x –C ORR electrocatalysis exploring the effect of two etching agents – NH_4HF_2 and NaF/HCl mixture – as in situ forming HF agents and avoiding the direct use of the most hazardous HF and thus opening the way for the sustainable production of ORR electrocatalysts.

Results and Discussion

Electrocatalysts Structure and Morphology

This study deals with the development of a more sustainable hard templating removal procedure for the preparation of Fe– N_x –C ORR electrocatalysts, where Silica-iron NPs (SFe) were simultaneously used as sacrificial supports to induce the micro- and meso-porosity while homogeneously dispersing iron in the Fe– N_x –C structure.^[80] The structure and composition of silica SFe NPs are in agreement with our previous study,^[80] as reported in Figure S1. Compared to the current technology, which entails the use of HF as an etching agent for the removal of SiO_2 -based templating agents, in this new approach, two different in situ HF forming agents were tested: i) NH_4HF_2 and ii) NaF + HCl. This strategy was recently proposed by Gentile *et al.* during the production of MXene^[81] but it was never proposed for SSM Fe– N_x –C family ORR electrocatalysts. Samples were named SFe–Y–X where Y is the etching agent and X the ratio between the etching agent and the silica. SFe–P1 is the electrocatalyst that was subject to the first controlled pyrolysis but did not undergo silica etching.

The effective removal of SiO_2 NPs was deeply investigated by using several techniques, including ATR-FTIR, TGA, XRF, and TEM analyses. ATR-FTIR spectra of SFe–Y in comparison to SFe–P1 (Figure 1a) first evidence that these salts are efficient in the etching process of SiO_2 : the typical features of SiO_2 , whose main peak is due to the stretching of Si–O–Si bond ($\nu_{Si-O-Si}$) is located at 1060 cm^{-1} in SFe–P1, disappears after the etching treatment with both NH_4HF_2 and NaF at high amount ($X=5$). However, when smaller amounts of the two agents are used ($X=1$), only NH_4HF_2 maintains the same high performance, while just a reduction in the intensity of the SiO_2 peak is achieved with NaF.

Similar results are highlighted by XRF analysis (Figure 1b). For all samples the peaks due to Fe are detected at 6.41 KeV and 7.09 KeV,^[82] confirming the presence of iron within the electrocatalysts. Besides, the Si signal at 1.74 KeV^[82] is observed in SFe–P1, but it becomes imperceptible in the SFe–Y–X series.

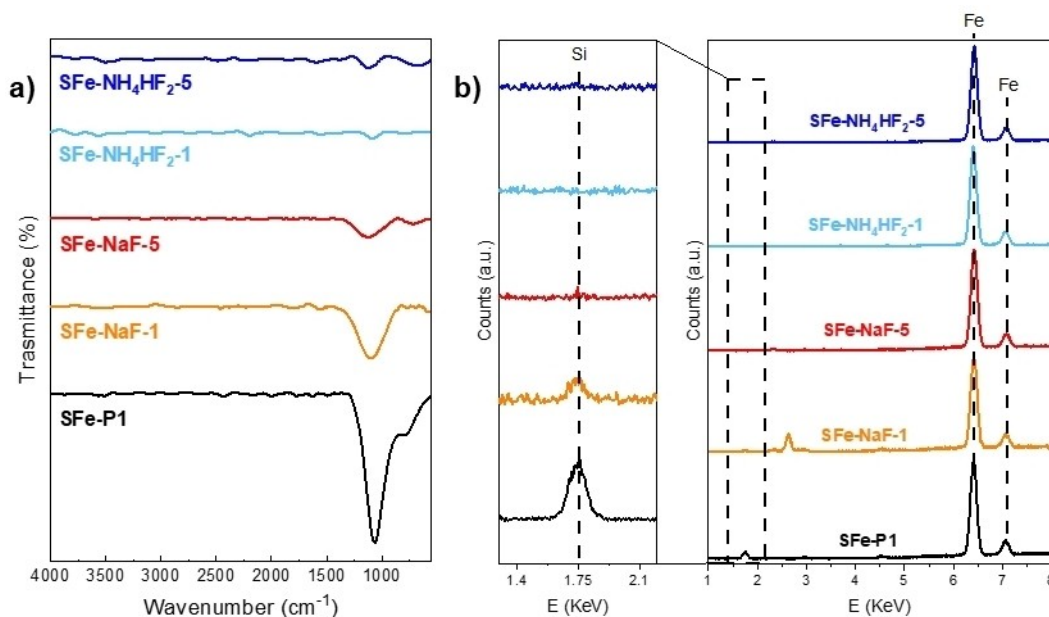


Figure 1. a) ATR-FTIR and b) XRF spectra obtained for SFe–Y–X materials in comparison to SFe–P1. Magnification of the the Si spectral region in highlighted in b).

Only for SFe–NaF–1, a tiny peak is still visible (zoom of Figure 1b), confirming that SiO₂ is only partially etched under these experimental conditions.

A quantification of SiO₂ removal was obtained by TGA analysis performed before and after the HF in situ formation treatment (Figure 2). In SFe–P1 the weight percentage due to silica is calculated by the sample weight (%) measured at 1000 °C, where only the inorganic component is still present, while the organic part has been eliminated through combustion.^[83] This corresponds to almost 50 wt% of SFe–P1,

which is equal to a mass ratio between the inorganic and organic part of 50:50; the reduced mass ratio compared to SFe–NC (30:70) is consistent with the degradation of the nitrogen-rich organic source (Nicarbazin) due to the first pyrolysis. Interestingly, the use of NH₄HF₂ at both molar ratios led to a complete removal of silica, as demonstrated by the tiny residual solid recovered at 1000 °C (<4 wt%). This remaining contribution accounts for the iron amount dispersed in SFe–Y–X materials, which is likely transformed into iron oxide species due to the TGA thermal treatment performed in the air. On the

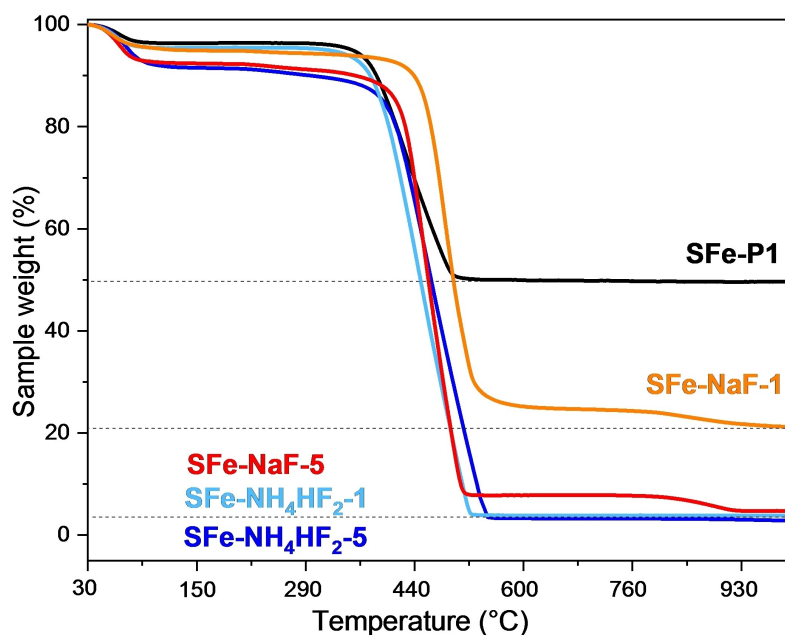
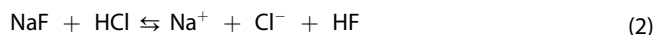


Figure 2. TGA curves of SFe–Y–X compared to that of SFe–P1.

contrary, only the use of an excess of NaF ($X=5$) led to similar results compared to NH_4HF_2 , whereas a significant amount of inorganic component (~ 20 wt %) is still measured at 1000°C for SFe-NaF-1, in agreement with the previous observations in the FTIR and XRF spectra.

These results indicate that both NH_4HF_2 and NaF are suitable precursors for the HF in situ formation, necessary for the silica etching, and thus representing potential substitutes to HF in the Fe-N_x-C preparation. In detail, these salts dissociate in aqueous solution through the following reactions:



giving rise to in situ HF formation. The so-formed dilute HF solutions generate the following equilibrium reaction:



where F^- and HF are then able to interact forming:



The equilibrium constant at 25°C of Equation (3) and Equation (4) are reported as $K_3 = 6.6 \times 10^{-4}$ and $K_4 = 3.9$, respectively.^[84] According to K_3 and K_4 , in the NH_4HF_2 solution, the most predominant fluoride species is represented by HF_2^- , which is formed from the reaction of HF and F^- ions, directly available from Equation (1). On the contrary, in the NaF solution, the similar concentration of both HF and HF_2^- should be present, as only little amounts of F^- are formed through Equation (3) compared to the NH_4HF_2 solution, due to the low K_3 . The diversity in the composition of the fluoride-based solutions could be herein used to explain the higher performances obtained with NH_4HF_2 at low content compared to NaF ($X=1$). Indeed, Judge et al. claimed that the dissolution rate of SiO_2 in dilute acidic fluoride solutions depends only on the concentration of HF_2^- and HF, whereas no influence of free fluoride was observed.^[85] Besides, they claim that the dissolution rate is about four to five times higher with HF_2^- compared to that obtained with HF. Verhaverbeke et al. further validated the previous model by Judge, also suggesting that a dimer of HF, $(\text{HF})_2$, is the other most important etching species together with HF_2^- ^[84] as only the occurrence of 2 or 4 fluorine atoms can initiate the etching process. No other species as $(\text{HF})_2\text{F}^-$, $(\text{HF})_3\text{F}^-$ or $(\text{HF})_4\text{F}^-$ are taken into account at low HF concentrations (< 1 M).^[86,87] More recently, new models also included the HF and F^- contribution to the silica etching process, still confirming the main role played by the negatively charged HF_2^- species.^[88] Thus, the likely higher HF_2^- concentration in the NH_4HF_2 solution could favor the kinetic of the etching process of SiO_2 . The discrepancy is almost eliminated by introducing higher amounts of the two etching agents.

In a nutshell, both NH_4HF_2 and NaF could represent potential turning points to reduce the overall hazard encountered in the Fe-N_x-C synthesis due to the direct use of HF and

prompt the large-scale production of Fe-N_x-C by simplifying the entire process and required facilities. Indeed, it must be stressed that even if the final obtained product is HF, the starting precursors are labeled as corrosive and toxic for ingestion (NH_4HF_2) and irritating (NaF), the HF is associated with much more severe risks as it is HF is defined as dangerous, fatal if swallowed, in contact with skin or inhaled and requires much stringent safety procedures when used in laboratory and industrial scale.

Later on, the morphological and structural investigation was centered on SFe- NH_4HF_2 -1 and SFe-NaF-5 samples, in which the lower amount of both agents was used with the highest performance for silica removal, to unveil their main features.

The structures of the two novel electrocatalysts were studied through XRPD, which show a broad peak at about 25° and a minor one at about 44° , due to the 002-oriented and 101-oriented diffraction peaks of graphite, respectively (Figure S2). No other features due to additional phases (i.e. amorphous silica) or impurities are detected, indicating a good homogeneity and purity of the materials at the end of the synthetic process.

The morphology of SFe-HF, SFe- NH_4HF_2 -1 and SFe-NaF-5 samples was investigated through TEM analyses (Figure 3). Images show for all the electrocatalysts the occurrence of homogeneous and continuous graphitic-based hollow structures made of holes, cavities and discontinuities generated from the removal of silica nanoparticles (Figure 3a-a'', b-b''). At higher magnifications the superimposition of several macro-microporous architectures (macropore size estimated from the images of about 65 ± 5 nm) can be appreciated along with the absence of any segregated or crystalline phase (Figure 3c-c', d-d').

The BET-specific surface area (SSA_{BET}) and pore-size distribution were determined by nitrogen physisorption. The samples show combined Type I-IV isotherms with narrow H3 hysteresis loop relatable to the presence of micro and mesopores in a macroporous network (Figure S3), in agreement with the hollow architecture observed from TEM images. Both SFe- NH_4HF_2 -1 and SFe-NaF-5 display large SSA_{BET} , namely 495 ± 2 m²g⁻¹ and 586 ± 2 m²g⁻¹, respectively. In both samples, the contribution of the micropores is relevant (see Table S1) and they represent the majority of the pore population (Figure S4). Conversely, SFe-HF exhibits a rather lower specific surface area (332 ± 2 m²g⁻¹) as well as a minor presence of micropores, as attested by the external surface area calculated by the t-plot method (Table S1).

Surface Chemistry

The surface chemistry of the electrocatalyst was thoroughly investigated by means of XPS. All the Fe-N_x-C samples show a similar surface atomic composition, with a carbon content of about 90.00 at. % and an oxygen content of around 5.50 at. %. The three electrocatalysts show a relatively high nitrogen doping (N at. % > 3.50), with the maximum value for the material based on the use of NH_4HF_2 (N at. % $= 4.10 \pm 0.20$). The

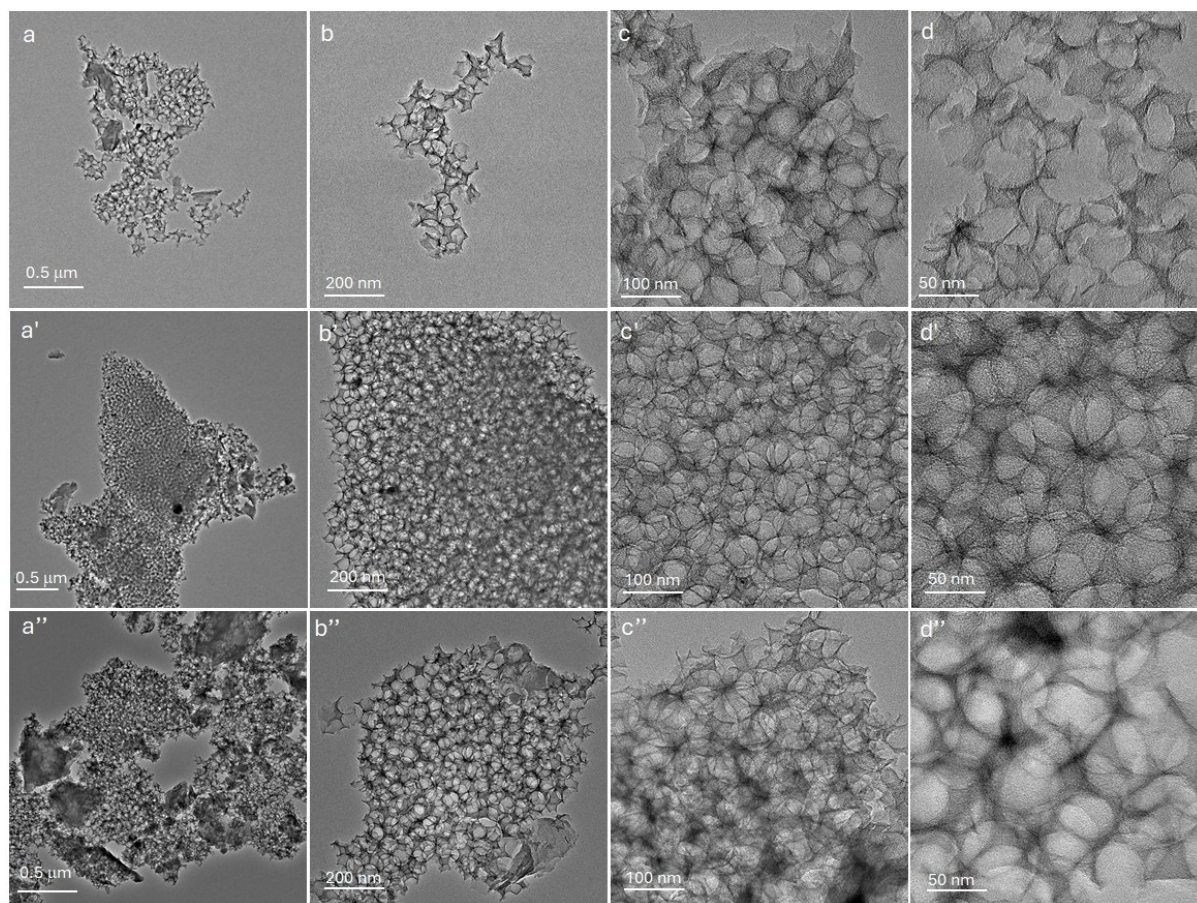


Figure 3. TEM images of SFe-HF (a-d), SFe-NH₄HF₂-1 (a'-d') and SFe-NaF-5 (a''-d'') at different magnifications.

detected amount of iron is relatively low (Fe at. % <0.20), but in line with previous studies from the literature.^[89,90] The results are summarized in Table 1.

Table 1. Surface atomic composition in at. % from XPS survey spectra.			
At. %	SFe-HF	SFe-NH ₄ HF ₂ -1	SFe-NaF-5
C 1 s	90.98 ± 0.10	89.99 ± 0.39	90.91 ± 0.25
N 1 s	3.52 ± 0.14	4.10 ± 0.20	3.76 ± 0.06
O 1 s	5.36 ± 0.04	5.84 ± 0.18	5.24 ± 0.36
Fe 2p _{3/2}	0.15 ± 0.01	0.08 ± 0.02	0.10 ± 0.05

Table 2. Surface relative composition of nitrogen moieties in relative at. % from XPS N 1s high-resolution spectra.			
Rel. At. %	SFe-HF	SFe-NH ₄ HF ₂ -1	SFe-NaF-5
N pyridinic	19.96 ± 0.09	23.66 ± 0.42	23.92 ± 0.82
N-Fe	14.80 ± 0.17	15.36 ± 0.53	10.36 ± 0.85
N pyrrolic	36.24 ± 0.20	34.67 ± 1.14	38.46 ± 0.11
N graphitic	12.05 ± 0.40	12.51 ± 1.76	13.44 ± 0.35
N quaternary	8.48 ± 0.18	6.64 ± 0.39	6.33 ± 1.21
NO _x	3.50 ± 0.08	4.04 ± 0.04	4.18 ± 0.30
NO _x	4.98 ± 0.39	3.14 ± 0.16	3.32 ± 0.30

The high-resolution N1s and C1s spectra were fitted according to previous works.^[68,89,91-93] From the nitrogen 1s detailed spectra, shown in Figure 4, several nitrogen moieties were identified: N pyridinic at 398.5 eV, Fe-nitrogen coordination at 399.4 eV, N pyrrolic at 400.8 eV, N graphitic at 401.8 eV, N quaternary at 403.2 eV and NO_x species at 404.4 eV and 405.9 eV. The N 1s relative atomic percentages are presented in Table 2.

The following carbon moieties were identified through the carbon 1s detailed spectra, presented in Figure 5: graphitic carbon at 284.5 eV, disordered carbon at 285.2 eV, C-N bond at 286.0 eV, C-O at 287.1 eV, C=O at 288.3 eV, COOH at 289.7 eV, C-F₂ at 291.3 eV and C-F₃ at 293 eV. The C 1s relative atomic percentages are summarized in Table 3.

The sample based on the use of HF (SFe-HF) shows the highest amount of iron and a relatively high content of N-Fe bond, reasonably resulting to be the material with the highest Fe-N_x active site density based on the XPS analysis. Instead, following the previous observation, the NaF-based electrocatalyst is the one with the lowest Fe-N_x active site density. ICP also showed a similar trend of iron content present in the samples as can be seen in Table S2. SFe-HF had maximum Fe present (2.49%) followed by SFe-NH₄HF₂-1 (1.93%) whereas the sample NaF-treated electrocatalyst had the lowest iron content (1.78%).

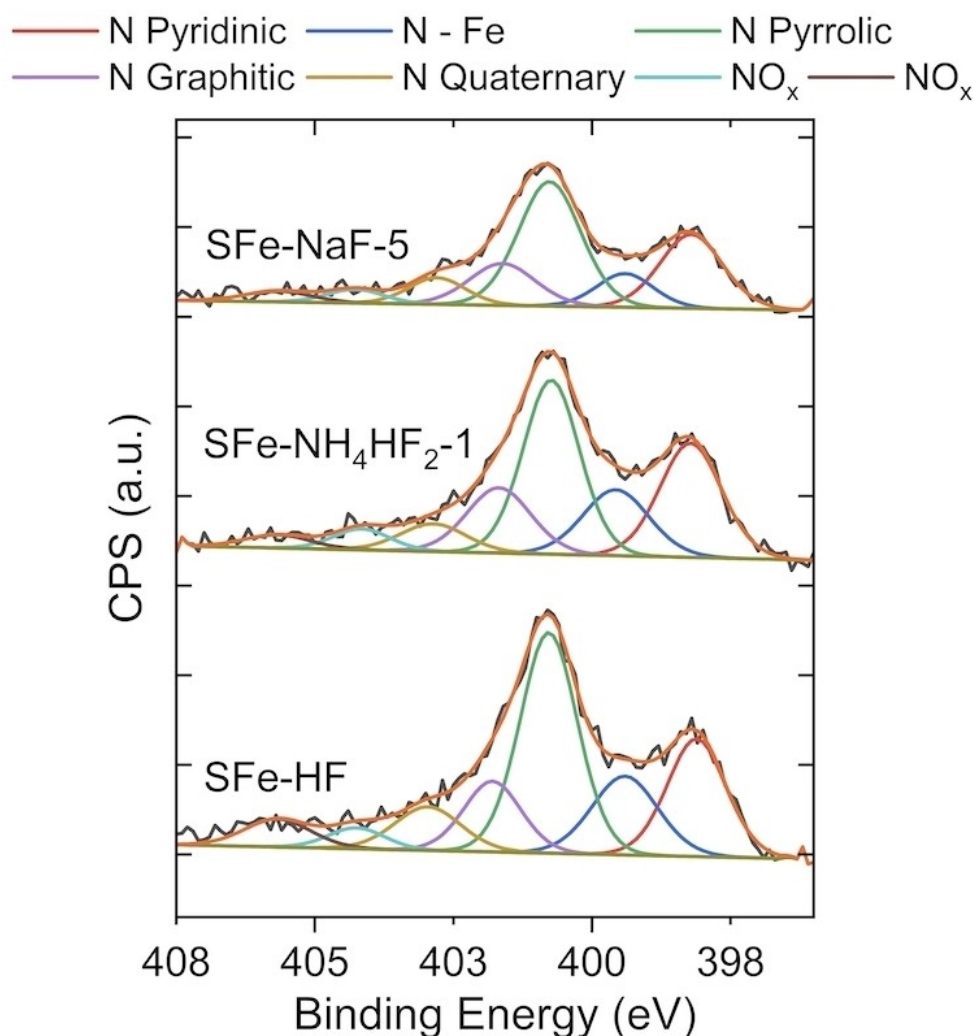


Figure 4. Detailed N 1s spectra of the three electrocatalysts synthesized: SFe-HF, SFe-NH₄HF₂-1, SFe-NaF-5

Table 3. Surface relative composition of carbon moieties in relative at. % from XPS C 1s high-resolution spectra.

Rel. At. %	HF	NH ₄ HF ₂	NaF
C graphitic	65.51 ± 0.17	62.59 ± 1.99	52.68 ± 4.53
C disordered	1.94 ± 0.44	10.18 ± 2.52	14.66 ± 3.36
C–N	9.70 ± 0.23	9.12 ± 0.23	13.81 ± 1.65
C–O	5.40 ± 0.61	5.86 ± 0.14	5.92 ± 0.27
C=O	5.26 ± 0.37	3.72 ± 0.58	3.80 ± 0.39
COOH	5.97 ± 0.09	4.81 ± 0.17	5.51 ± 0.32
C–F ₂	3.90 ± 0.11	2.51 ± 0.13	2.31 ± 0.43
C–F ₃	2.35 ± 0.08	1.23 ± 0.12	1.31 ± 0.25

Electrochemical Results

Oxygen Reduction Reaction in Acid Media

ORR electrocatalytic activity of the three electrocatalysts (SFe-HF, SFe-NH₄HF₂-1 and SFe-NaF-5) was evaluated in acidic

media, with the electrolyte being 0.5 M H₂SO₄. The linear sweep voltammetry was run from 1 V vs RHE to 0 V vs RHE at a rotating rate of 1600 rpm. Two electrocatalyst loadings were investigated, being 0.2 mg cm^{−2} and 0.6 mg cm^{−2}. Disk currents are presented in Figure 6a. Interestingly, the increase in electrocatalyst loading led to an increase in both potential onset and half-wave potential (Figure 6a). At lower electrocatalyst loading, SFe-NaF-5_0.2 had an E_{on} of 0.75 V (vs RHE) and an E_{1/2} of 0.55 V (vs RHE). Identical E_{on} but higher E_{1/2} (0.57 V vs RHE) was recorded for both SFe-NH₄HF₂-1_0.2 and SFe-HF_0.2. The limiting current (J_{lim}) for tests at 0.2 mg cm^{−2} electrocatalyst loading was in the range of 2.8 A cm^{−2} and 3.3 A cm^{−2}. At electrocatalyst loading of 0.6 mg cm^{−2}, the E_{on} varied between 0.81 V vs RHE (SFe-NH₄HF₂-1_0.6) and 0.85 V vs RHE (SFe-HF_0.6). The E_{1/2} varied between 0.63 V vs RHE (SFe-HF_0.6) to 0.65 V vs RHE (SFe-NH₄HF₂-1_0.6) and 0.71 V vs RHE (SFe-NaF-5_0.6). The higher J_{lim} was recorded with SFe-NH₄HF₂-1_0.6 and it was 4.4 mA cm^{−2}. Ring current density was recorded and presented in Figure 6b. From the ring current density, it was possible to determine the peroxide produced (Figure 6c) that varied between 4% and 15% at potentials below 0.4 V vs RHE. The

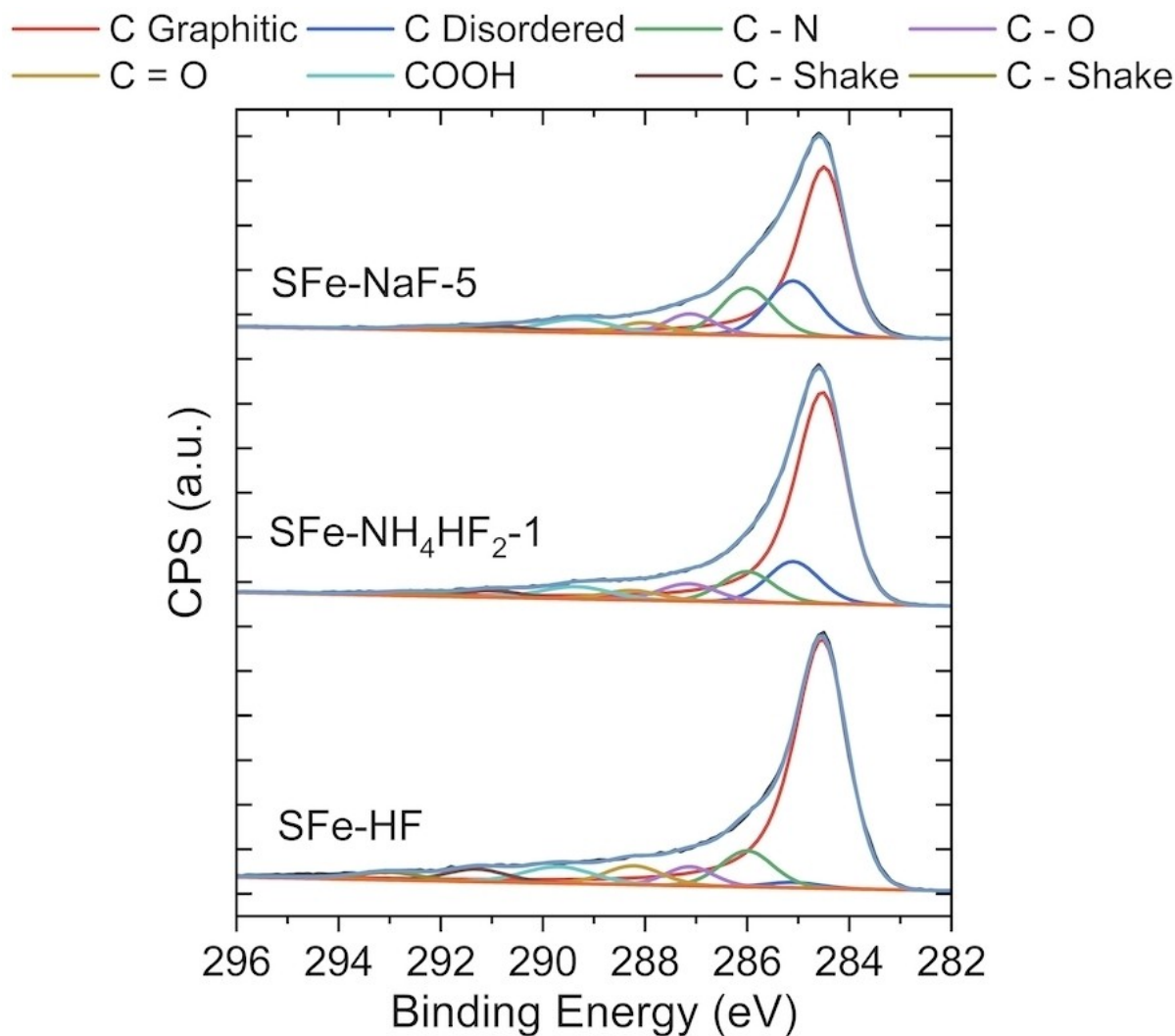


Figure 5. Detailed C 1s spectra of three electrocatalysts synthesized: SFe-HF, SFe-NH₄HF₂-1, SFe-NaF-5

increase in electrocatalyst loading led to a decrease in peroxide produced indicating that the peroxide is consumed within the thicker electrocatalyst layer. The number of electrons transferred was always above 3.7 (Figure 6d). This indicates that the ORR occurs mainly over a direct 4-electron transfer.

Oxygen Reduction Reaction in Alkaline Media

The electrocatalytic activity of Fe-N_x-C electrocatalysts in alkaline media is higher compared to the one in acid media^[94,75] and this was shown also in this case (Figure 7). Disk current is presented in Figure 7a, ring current is shown in Figure 7b, peroxide production is displayed in Figure 7c and transferred electrons are presented in Figure 7d. E_{on} and $E_{1/2}$ increased with the electrocatalyst loading.

SFe-NH₄HF₂-1 had higher results compared to the other electrocatalysts in both loadings. Particularly, SFe-NH₄HF₂-1_0.2 showed an E_{on} of 0.94 V vs RHE and $E_{1/2}$ of 0.85 V vs RHE. At 0.6 mg cm⁻², SFe-NH₄HF₂-1_0.6 had an E_{on} of 0.97 V vs RHE and

$E_{1/2}$ of 0.88 V vs RHE. Interestingly, at the loading of 0.2 mg cm⁻², SFe-NaF-5_0.2 outperformed SFe-HF_0.2, but at higher loading, SFe-HF_0.6 had slightly higher electrocatalytic activity compared to SFe-NaF-1_0.6 (Figure 7a). A lower peroxide generation was recorded by SFe-NaF-5 followed by SFe-NH₄HF₂-1 and SFe-HF, for which the highest peroxide yield was detected (Figure 7c). The higher number of electrons transferred was achieved by SFe-NaF-5 and SFe-NH₄HF₂-1 samples (Figure 7d). Higher electrocatalyst loading led to a higher number of transferred electrons as lower peroxide was detected due to its reduction within the electrocatalyst layer. In general, despite the loading, in alkaline media, the removal of silica through NH₄HF₂ results in electrocatalysts with superior features compared to those obtained after etching with HF.

While coming to the point, it is important to highlight that both reagents i.e. NaF and NH₄HF₂ proved to be very effective in dissolving the silica templates while maintaining the architectural features and corresponding electrocatalytic activity similar or even superior to that treated by HF. Compared to NaF, five times less NH₄HF₂ was consumed to remove silica.

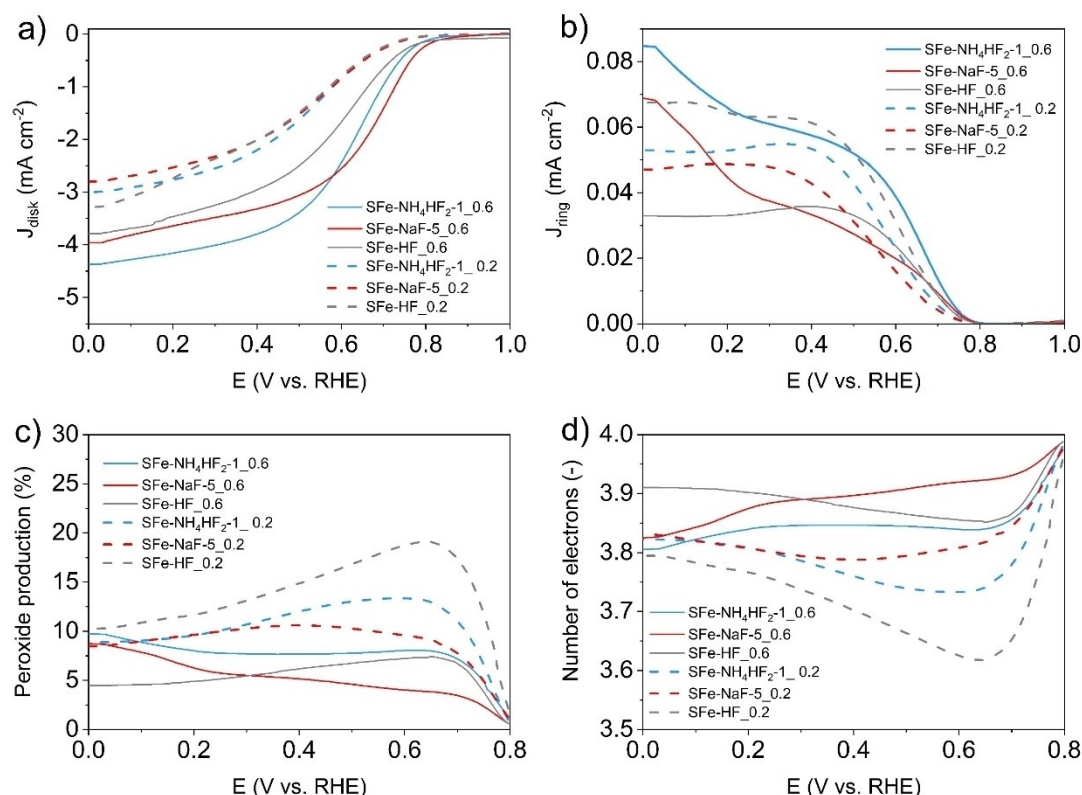


Figure 6. Disk Current density (a), Ring Current density (b), Peroxide produced (c) and Electrons transferred (d) for electrocatalyst etched using HF (grey lines), NaF (red lines) and NH_4HF_2 (light blue lines). Two loadings were explored, 0.2 mg cm^{-2} (dot line) and 0.6 mg cm^{-2} (continuous line). Tests were done in $0.5 \text{ M H}_2\text{SO}_4$ with a rotating speed of 1600 rpm .

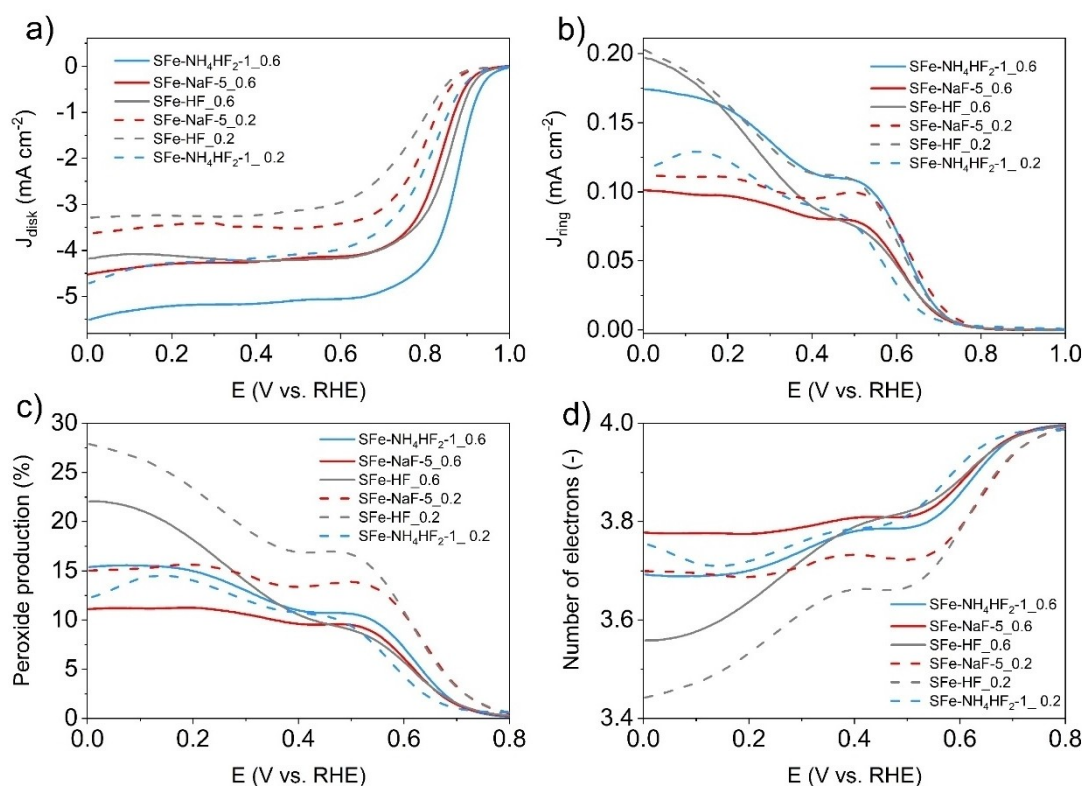


Figure 7. Disk Current density (a), Ring Current density (b), Peroxide produced (c) and Electrons transferred (d) for electrocatalyst etched using HF (grey lines), NaF (red lines) and NH_4HF_2 (light blue lines). Two loadings were explored, 0.2 mg cm^{-2} (dot line) and 0.6 mg cm^{-2} (continuous line). Tests were done in 0.1 M KOH with a rotating speed of 1600 rpm .

Moreover, the NH_4HF_2 -treated sample kinetically outperformed the other counterpart (NaF-treated) by realizing higher ORR E_{on} and $E_{1/2}$ in both electrolytic media i.e. acidic and alkaline. However, the activity was clearly enhanced under alkaline conditions which is aligned with the ultimate goal of AEMFC applications. The peak ORR kinetic activity i.e. E_{on} and $E_{1/2}$ can be linked with the relative higher proportion of Fe–N_x in the NH_4HF_2 -treated sample as revealed by XPS. Fe–N_x are known as the primary active sites for the ORR.^[43,95,96] Also ICP confirmed the higher iron content in the NH_4HF_2 -treated sample than the NaF-treated sample. Moreover, TEM illustrated the well-defined mesoporous graphitic structure without large-scale coalescence of Fe-type species into metallic nanoparticles, especially for the SFe– NH_4HF_2 –1 sample. Additionally, SFe– NH_4HF_2 –1 exhibited a BET surface area that was considerably higher than that of the HF-treated sample. On the other hand, a slightly higher content of graphitic nitrogen could be a cause of delaying the E_{on} and $E_{1/2}$ of the NaF-etched sample.^[97] However, a slightly higher surface area of the NaF-treated sample might ensure enhanced accessibility to the active moieties and could be the reason behind the marginally lower peroxide yield. Nevertheless, it should be noted that five times more NaF was required to effectively remove silica templates which could be a limitation. In any case, the performance of the NH_4HF_2 -treated sample outperformed the other counterparts in terms of activity while following a nearly tetra-electronic pathway and keeping the peroxide yield below ~10% and ~15% in acidic and alkaline media, respectively.

Comparisons with Existing Literature

The results presented are in line and sometimes outperform the best PGM-free electrocatalysts shown in literature for oxygen reduction reactions. In Table 4, a few examples of electrocatalysts tested using SSM and removal of the hard templating using HF are reported. Commercially available Fe–N_x–C electrocatalysts are also compared.

Outlook Towards Sustainable Large-Scale ORR Electrocatalysts

In this work, Fe–N_x–C-type electrocatalysts were synthesized through the sacrificial support method (SSM). The main variation was the removal of the hard templating with different agents. While HF is generally used for this procedure, the utilization of other agents that can produce HF in situ is novel and not yet explored. The usage of HF is considered a critical bottleneck for the SSM synthetic procedure because HF is extremely difficult to handle, it is extremely volatile and if not handled properly it can cause extremely severe health injuries and environmental issues. Therefore, alternative solutions that are also more sustainable have to be considered. In this work, the etching was conducted also with NaF and NH_4HF_2 . While the etching with NaF was done by mixing NaF with HCl, a water solution containing NH_4HF_2 was used limiting the handle of dangerous agents. Even HBF_4 was used in this work (data not shown), however the removal of silica was extremely poor. In this study, the etching using an aqueous solution containing NH_4HF_2 was more effective than using HF and this was proven by higher N_x–Fe relative percentage (primary active sites) and by the higher percentage of N-pyridinic (secondary active sites)

Table 4. Comparison with recent studies involving the etching of silica templates to form ORR electrocatalysts.

Electrocatalysts	Etching Agent	E_{on} (V vs RHE)	$E_{1/2}$ (V vs RHE)	Peroxide (%)	Electrons Transfer	Electrolyte	Catalyst Loading (mg cm^{-2})	Ref.
$\text{Fe}_{\text{A0}}\text{--N--C}^{\text{AF}}$	Teflon powder	0.9	0.81	1.10	3.9	0.1 M KOH	0.6	[89]
FeNSC	HF solution	0.97	0.87	-	3.98	0.1 M KOH	0.67*	[98]
HPC–Fe/N-700	NaOH	0.92	0.84	5.4	3.89	0.1 M KOH	0.24	[99]
Ordered mesoporous carbon	NaOH	0.83	0.75	25	2.4	0.1 M KOH	0.2	[100]
Co–TpBpy-800	6 M KOH	0.91	0.83	-	ca. 3.9	0.1 M KOH	0.25	[101]
Si–Fe–N/C	HF solution	-	0.83	3.35	ca. 3.9	0.1 M KOH	ca. 0.6	[102]
NFe-PG	NaOH solution	1.00	0.84	-	3.87–3.99	0.1 M KOH	0.04	[103]
Fe(0)/FeN _x –NC-7	HF solution	0.95	0.86	≤ 12.3	3.72–3.9	0.1 M KOH	ca. 0.3	[104]
FeNC_PME	HF solution	~0.83	0.75	ca. ≥ 30	3–3.5	0.1 M KOH	0.6	[105]
SEFe_M_P1AP2	HF solution	0.96	0.88	ca. ≤ 14.5	ca. 3.7–3.9	0.1 M KOH	0.6	[80]
(FeCo)HPNC@NaCl	3 M KOH	-	0.81	-	3.92	0.1 M HClO_4	0.51	[106]
NSMC 0.4	2 M NaOH	0.78	0.68	81	1.8	0.1 M KOH	0.204	[107]
2%Fe–ZIF@NaCl	HCl	0.96	0.83	-	ca. 4	0.1 M HClO_4	0.8	[108]
FeCo-OMPC	10% HF	1.00	0.85	-	3.9	0.1 M HClO_4	0.6	[109]
SFe– NH_4HF_2 –1_0.6	NH_4HF_2	0.97	0.88	≤ 15	≥ 3.81	0.1 M KOH	0.6	This work
SFe– NH_4HF_2 –1_0.6	NH_4HF_2	0.81	0.65	< 10	> 3.8	0.5 M H_2SO_4	0.6	This work

*Estimated Electrocatalyst Loading.

compared to the other two electrocatalysts tested. Moreover, the NH_4HF_2 etched electrocatalyst showed similar performance compared to HF in acid media but superior electrocatalytic activity in alkaline media.

Experimental Section

Materials

For the synthesis of silica templates: tetraethylorthosilicate (TEOS), ammonium hydroxide (NH_4OH 25%) and iron sulphate heptahydrate $\text{Fe}_2(\text{SO}_4)_3 \cdot 7\text{H}_2\text{O}$ were purchased from Merck Life Science (Germany). N-aminoethyl-aminopropyltriethoxysilane (EDTMS) and Ethanol (EtOH, 99.8%) were obtained from abcr Gute Chemie (Germany) and Exacta Optech LabCenter (Italy), respectively. For the electrocatalyst preparation, nicarbazin (NC), ammonium hydrogen difluoride (NH_4HF_2 , 95%), sodium fluoride (NaF, $\geq 99\%$) and hydrochloric acid (HCl, 37% v/v) were acquired from Merck Life Science (Germany). Milli-Q water was produced by a Milli-Q Essential apparatus.

Electrocatalyst Synthesis

The electrocatalysts were prepared by means of the hard template approach, using functionalized SiO_2 NPs as sacrificial supports for the dispersion of iron active centers and to induce the micro- and meso-porosity into the electrocatalyst structure.^[80] Briefly, SiO_2 NPs (average diameter 70 ± 5 nm) were prepared through a Stöber method^[110,111] and surface functionalized by the hydrolysis and condensation of EDTMS with the surface -OH groups of SiO_2 NPs (molar ratio between silane: OH groups of SiO_2 equal to 1:2). Then, the terminal amino groups of EDTMS were exploited to disperse single iron sites (using $\text{Fe}_2(\text{SO}_4)_3 \cdot 7\text{H}_2\text{O}$ as iron precursor) onto the SiO_2 surface (Fe: EDTMS molar ratio equal to 1.5:1). The final material was labeled as SFe and used to synthesize $\text{Fe-N}_x\text{-C}$ electrocatalysts.

SFe was mixed with a nitrogen-rich organic molecule, in this case Nicarbazin, with a mass ratio equal to 30:70, in Milli-Q water (100 mL/g_{SFe}) for 24 h at room temperature (RT). The dried material was pyrolyzed (SFe-P1) at 900 °C under pure N_2 for 1 h, using a heating and cooling rate of 300 °C h⁻¹. Then, the mixtures were etched in Teflon labware to remove the silica sacrificial supports by testing two aqueous solutions of different in situ HF forming agents as recently shown:^[81] i) NH_4HF_2 (10 wt%) and ii) NaF + HCl (8.5 wt% and 18 wt%, respectively). The amount of the etching solutions has been calculated according to three parameters:

- the quantity of HF formed from the dissolution of NH_4HF_2 and NaF in water (Equation(1–2)), that corresponds to 1 mol of HF for each mole of tested etching agent. According to Equation (3–4) and to the values of $K_3\text{-}K_4$, this amount will mostly correspond to the moles of HF_2^- in solution in the case of NH_4HF_2 solution, while a mixture of HF, F^- , HF_2^- and dimers of $(\text{HF})_2$ will form in the NaF solution;

- the amount of SiO_2 in SFe-P1 measured by Thermogravimetric Analysis (TGA);
- the overall dissolution reaction of SiO_2 by HF, which requires six moles of F^- for each Si mole to produce the hexafluoro-silicic acid (H_2SiF_6) during the etching process.^[84,112]

For the tests, both a stoichiometric amount (1x) and an excess of the two agents (5x, correspondent to five times the stoichiometric amount) were used, correspondent to a molar ratio between the in situ formed HF and SiO_2 equal to 6 and 30, respectively. In a typical procedure, the etching solutions were slowly mixed with SFe-P1 at 40 °C and kept under stirring in an oil bath for 24 h. Later on, the samples were recovered through centrifugation (9000 rpm, 30 min) and washed several times with water until the pH of the supernatant became neutral. The powders were dried at 80 °C overnight and finally pyrolyzed a second time under a slightly reducing atmosphere of N_2/H_2 95/5 wt% at 900 °C for 1 h, with a heating and cooling rate of 300 °C h⁻¹. The final samples were labeled as SFe-Y-X, where Y is the used HF forming agent for silica removal and X is the amount used of each agent, equal to 1 or 5, for the stoichiometric amount and the excess, respectively.

Reference Fe-N_x-C sample for the electrochemical tests was prepared by following the same procedure herein described but using a HF/HNO₃ mixture for the silica etching process (2:1 mixture of HF 25 wt% and HNO₃ 35 wt%, RT, 3 days), according to Honig et al.^[80]

Electrocatalyst Characterization

Infrared Spectroscopy (FTIR) in the Attenuated Total Reflectance (ATR) mode was carried out using a Thermo Fisher Scientific Nicolet iS20 instrument. FTIR spectra were collected between 4000–550 cm⁻¹, with a 1 cm⁻¹ resolution, 32 scans. **Thermogravimetric analysis (TGA)** was performed by using a Mettler Toledo StarE system TGA/DSC1 instrument (scan range 30–1000 °C, heat rate 10 °C min⁻¹, constant air flow 50 mL min⁻¹). Both FTIR spectra and TGA curves were registered on bare SFe to assess the successful SiO_2 functionalization, as well as on SFe-Y samples to verify the effective silica removal by the HF forming agents compared to SFe-P1. This was further verified by **X-ray Fluorescence (XRF)** with a Bruker EDXRF spectrometer (Artax 200) equipped with an X-ray tube (Mo anode) with a beam collimated down to 0.65 mm in diameter (excited sample area of 0.33 mm²). The working conditions were 20 kV and 1.0 mA with an acquisition time of 300 seconds.

Transmission Electron Microscopy (TEM) images collected at low magnification were used to confirm the absence of silica particles on SFe-Y. TEM analysis was performed with a JEOL JEM-2100Plus TEM operating with an acceleration voltage of 200 kV, equipped with an 8-megapixel Gatan RioTM complementary metal-oxide-semiconductor camera. The samples were deposited onto carbon coated Cu TEM mesh grids by drop-casting dilute NPs dispersions in EtOH.

Inductively Coupled Plasma-Optical Emission spectroscopy (ICP-OES) was used to measure the iron amount in SFe, with an

ICP-OES Optima 7000 DV Perkin Elmer instrument, after the acid digestion in a microwave Milestone Ethos mineralizer.

The structure of SFe–Y electrocatalysts was studied with the *X-Ray Powder Diffraction (XRPD)*, by using a Rigaku MiniFlex 600 diffractometer with 1.5406 Å Cu K α radiation, in the 2 θ range between 5–80°, 2 θ step 0.02°, 1° min^{−1} scan rate. *Specific surface area (SSA)*, desorption cumulative pore volume (DCPV) and pore size distribution were measured with a Quantachrome Autosorb iQ–C instrument, where nitrogen was employed as the adsorbate at 77 K, according to BET. The samples were previously evacuated at 80°C for 30 min, 120°C for other 30 min and finally at 350°C for 7 h before the analysis. The pore size distribution was calculated using the DFT method for slit pores. The surface chemical environment and composition of the materials were examined using *X-ray photoelectron spectroscopy (XPS)* on a Kratos AXIS Supra machine with a focused Al K α beam (1486.6 eV) at 15 mA and 225 W. Data was gathered from 0 to 1400 eV for survey scans, 270 to 300 eV for C 1s detailed scans, 390 to 415 eV for N 1s detailed scans, 702 to 740 eV for Fe 2p detailed scans, and 525 to 543 eV for O 1s detailed scans.

The software CasaXPS was employed for elemental analysis of the surface. A linear background was used for C 1s, N 1s, and O 1s, while a Shirley background was applied to the Fe 2p 3/2 region. Gaussian/Lorentzian peak (70%/30%) was chosen for peak analysis.

Electrochemical Characterization

Linear sweep voltammetry in a three-electrode cell (Pine WaveVortex RDE system coupled with a Pine potentiostat) was used to study the ORR electrochemical activity of the samples. The working electrode was a rotating ring disk electrode (RRDE) with the geometric area of the glassy carbon disk equal to 0.2376 cm² and the platinum ring geometric area of 0.2356 cm². The rotation speed of the working electrode was set to 1600 rpm. An SSG was immersed into the electrolyte solution and used as a reference electrode. The counter electrode was a titanium spring. The inks were prepared by tip sonication 5 mg of the catalyst in a solution made of 985 μ L of isopropanol and 15 μ L of Nafion® 5% dispersion in water/ethanol. The obtained ink was deposited over the glassy carbon by drop casting. Before the measurements, the electrolyte was saturated with oxygen by flowing it for 20 min in the solution. In order to maintain the solution saturated with oxygen, a minimum flow of oxygen was maintained also during measurements. The potential scan range was from 1 V to 0 V versus RHE. All measured potentials were converted to potential versus RHE according to Equation (1).

$$E_{\text{RHE}} = E_{\text{SSG}} + 0.059 \cdot \text{pH} + E_{\text{SSG}}^0 \quad (1)$$

The potential of the ring was fixed at 1 V versus RHE. The currents generated at the disk (I_d) and the ring (I_r) were used to calculate the hydrogen peroxide anion produced and the

number of electrons transferred (n) respectively following the Equation (2) and (3):

$$\text{Peroxide, \%} = \frac{200 \cdot \frac{I_r}{N}}{I_d + \frac{I_r}{N}} \quad (2)$$

$$n = \frac{4I_d}{I_d + \frac{I_r}{N}} \quad (3)$$

N is the collection efficiency of the ring, it was reported by the supplier as 38%.

Acknowledgements

C.S. would like to acknowledge the NextGeneration EU from the Italian Ministry of Environment and Energy Security POR H2 AdP MMES/ENEA with involvement of CNR and RSE, PNRR - Mission 2, Component 2, Investment 3.5 "Ricerca e sviluppo sull'idrogeno" under the ENEA – UNIMIB agreement (Procedure 1.1.3 PNRR POR H2). C.S. would like to also acknowledge the Cariplo Foundation, Call for Circular Economy through the project "Transformation of plastic waste in Electrocatalysts, Supported by exhausted gases recovery Layout" (TESLA). G.Z. acknowledges a Ph.D. scholarship on the Italian National Ph.D. program "Scientific, technological and social methods enabling circular economy", Curriculum "Technical materials for circularity" funded by Italy's Recovery and Resilient Plan and EU Recovery Plan. Open Access publishing facilitated by Università degli Studi di Milano-Bicocca, as part of the Wiley - CRUI-CARE agreement.

Conflict of Interests

The authors declare no conflict of interest.

Data Availability Statement

The data that support the findings of this study are available from the corresponding author upon reasonable request.

Keywords: Oxygen reduction reaction • Sacrificial support method • Avoid HF • Alkaline media electrolyte • Acidic media electrolyte

- [1] T. Ioroi, Z. Siroma, S. Yamazaki, K. Yasuda, *Adv. Energy Mater.* **2019**, *9*, 1801284.
- [2] S. Zhang, Y. Shao, G. Yin, Y. Lin, *J. Mater. Chem. A* **2013**, *1*, 4631.
- [3] L. Su, W. Jia, C. M. Li, Y. Lei, *ChemSusChem* **2014**, *7*, 361–378.
- [4] Y. He, Q. Tan, L. Lu, J. Sokolowski, G. Wu, *Electrochem. Energy Rev.* **2019**, *2*, 231–251.
- [5] E. Marra, H. Grimler, G. Montserrat-Sisó, R. W. Lindström, B. Wickman, G. Lindbergh, C. Lagergren, *Electrochim. Acta* **2022**, *435*, 141376.
- [6] J. Zhao, C. Fu, K. Ye, Z. Liang, F. Jiang, S. Shen, X. Zhao, L. Ma, Z. Shadike, X. Wang, J. Zhang, K. Jiang, *Nat. Commun.* **2022**, *13*, 685.
- [7] A. M. Gómez-Marín, J. M. Feliu, *ChemSusChem* **2013**, *6*, 1091–1100.

- [8] J. Bai, S. Ke, J. Song, K. Wang, C. Sun, J. Zhang, M. Dou, *ACS Appl. Mater. Interfaces* **2022**, *14*, 5287–5297.
- [9] Y. Lv, H. Liu, J. Li, J. Chen, Y. Song, *J. Electroanal. Chem.* **2020**, *870*, 114172.
- [10] L. Fan, H. Deng, Y. Zhang, Q. Du, D. Y. C. Leung, Y. Wang, K. Jiao, *Energy Environ. Sci.* **2023**, *16*, 1466.
- [11] H. Schmies, T. Zierdt, J. Mueller-Huelstede, W. Deter, J. Lorenz, M. Wark, P. Wagner, *J. Power Sources* **2022**, *529*, 231276.
- [12] H. Tang, K. Geng, D. Aili, Q. Ju, J. Pan, G. Chao, X. Yin, X. Guo, Q. Li, N. Li, *Nat. Commun.* **2022**, *13*, 7577.
- [13] Y. Sun, S. Polani, F. Luo, S. Ott, P. Strasser, F. Dionigi, *Nat. Commun.* **2021**, *12*, 5984.
- [14] Q. Meyer, C. Yang, Y. Cheng, C. Zhao, *Electrochem. Energy Rev.* **2023**, *6*, 16.
- [15] F. Zhu, L. Luo, A. Wu, C. Wang, X. Cheng, S. Shen, C. Ke, H. Yang, J. Zhang, *ACS Appl. Mater. Interfaces* **2020**, *12*, 26076–26083.
- [16] H. Cruz-Martínez, H. Rojas-Chávez, P. T. Matadamas-Ortiz, J. C. Ortiz-Herrera, E. López-Chávez, O. Solorza-Feria, D. I. Medina, *Mater. Today Phys.* **2021**, *19*, 100406.
- [17] X. Wei, R. Z. Wang, W. Zhao, G. Chen, M. R. Chai, L. Zhang, J. Zhang, *EnergyChem* **2021**, *3*, 100061.
- [18] E. Zhu, M. Wu, H. Xu, B. Peng, Z. Liu, Y. Huang, Y. Li, *Adv. Funct. Mater.* **2022**, *32*, 2203883.
- [19] A. Ali, A. Laaksonen, G. Huang, S. Hussain, S. Luo, W. Chen, P. K. Shen, J. Zhu, X. Ji, *Nano Res.* **2024**, *17*, 3516–3532.
- [20] C. Qin, S. Tian, W. Wang, Z. J. Jiang, Z. Jiang, *Front. Chem.* **2022**, *10*, DOI: 10.3389/fchem.2022.1073566.
- [21] J. Cui, Q. Chen, X. Lid, S. Zhang, *Green Chem.* **2021**, *23*, 6898.
- [22] E. F. Holby, G. Wang, P. Zelenay, *ACS Catal.* **2020**, *10*, 14527–14539.
- [23] Y. He, G. Wu, *Acc. Mater. Res.* **2022**, *3*, 224–236.
- [24] K. Kumar, L. Dubau, F. Jaouen, F. Maillard, *Chem. Rev.* **2023**, *123*, 9265–9326.
- [25] J. R. Varcoe, P. Atanassov, D. R. Dekel, A. M. Herring, M. A. Hickner, P. A. Kohl, A. R. Kucernak, W. E. Mustain, K. Nijmeijer, K. Scott, T. Xu, L. Zhuang, *Energy Environ. Sci.* **2014**, *7*, 3135.
- [26] D. R. Dekel, *J. Power Sources* **2018**, *375*, 158–169.
- [27] S. Gottesfeld, D. R. Dekel, M. Page, C. Bae, Y. Yan, P. Zelenay, Y. S. Kim, *J. Power Sources* **2018**, *375*, 170–184.
- [28] M. M. Hossen, M. S. Hasan, M. R. I. Sardar, J. bin Haider, Mottakin, K. Tammeveski, P. Atanassov, *Appl. Catal. B: Environ.* **2023**, *325*, 121733.
- [29] X. Huang, T. Shen, T. Zhang, H. Qiu, X. Gu, Z. Ali, Y. Hou, *Adv. Energy Mater.* **2020**, *10*, 1900375.
- [30] G. Wu, A. Santandreu, W. Kellogg, S. Gupta, O. Ogoke, H. Zhang, H. L. Wang, L. Dai, *Nano Energy* **2016**, *29*, 83–110.
- [31] G. Wu, P. Zelenay, *Acc. Chem. Res.* **2013**, *46*, 1878–1889.
- [32] L. Osmieri, *ChemEngineering* **2019**, *3*, 16.
- [33] A. Sarapu, J. Lilloja, S. Akula, J. H. Zagal, S. Specchia, K. Tammeveski, *ChemCatChem* **2023**, *15*, e202300849.
- [34] C. Santoro, P. Bollella, B. Erable, P. Atanassov, D. Pant, *Nat. Catal.* **2022**, *5*, 473–484.
- [35] S. Gupta, S. Zhao, O. Ogoke, Y. Lin, H. Xu, G. Wu, *ChemSusChem* **2017**, *10*, 774–785.
- [36] D. Sebastian, A. Serov, K. Artyushkova, J. Gordon, P. Atanassov, A. S. Aricò, V. Baglio, *ChemSusChem* **2016**, *9*, 1986–1995.
- [37] M. Muhyuddin, E. Berretti, S. A. Mirshokraee, J. Orsilli, R. Lorenzi, L. Capozzoli, F. D'Acapito, E. Murphy, S. Guo, P. Atanassov, A. Lavacchi, C. Santoro, *Appl. Catal. B: Environ.* **2024**, *343*, 123515.
- [38] J. Zou, C. Chen, Y. Chen, Y. Zhu, Q. Cheng, L. Zou, Z. Zou, H. Yang, *ACS Catal.* **2022**, *12*, 4517–4525.
- [39] B. Jeong, D. Shin, H. Jeon, J. D. Ocon, B. S. Mun, J. Baik, H. J. Shin, J. Lee, *ChemSusChem* **2014**, *7*, 1289–1294.
- [40] N. Ramaswamy, S. Mukerjee, *J. Phys. Chem. C* **2011**, *115*, 18015–18026.
- [41] H. Shen, T. Thomas, S. A. Rasaki, A. Saad, C. Hu, J. Wang, M. Yang, *Electrochem. Energy Rev.* **2019**, *2*, 252–276.
- [42] X. Ge, A. Sumboja, D. Wu, T. An, B. Li, F. W. T. Goh, T. S. A. Hor, Y. Zong, Z. Liu, *ACS Catal.* **2015**, *5*, 4643–4667.
- [43] K. Artyushkova, A. Serov, S. Rojas-Carbonell, P. Atanassov, *J. Phys. Chem. C* **2015**, *119*, 25917–25928.
- [44] S. A. Mirshokraee, M. Muhyuddin, J. Orsilli, E. Berretti, A. Lavacchi, C. Lo Vecchio, V. Baglio, R. Viscardi, A. Zaffora, F. Di Franco, M. Santamaria, L. Olivi, S. Pollastri, C. Santoro, *Nanoscale* **2024**, *16*, 653.
- [45] G. Zuccante, M. Acciarri, C. Lo Vecchio, I. Gatto, V. Baglio, N. Pianta, R. Ruffo, L. Navarini, C. Santoro, *Electrochim. Acta* **2024**, *492*, 144353.
- [46] M. Muhyuddin, A. Friedman, F. Poli, E. Petri, H. Honig, F. Basile, A. Fasolini, R. Lorenzi, E. Berretti, M. Bellini, A. Lavacchi, L. Elbaz, C. Santoro, F. Soavi, *J. Power Sources* **2023**, *556*, 232416.
- [47] S. Akula, M. Mooste, J. Kozlova, M. Käärik, A. Treshchalov, A. Kikas, V. Kisand, J. Aruväli, P. Päärn, A. Tamm, J. Leis, K. Tammeveski, *J. Chem. Eng.* **2023**, *458*, 141468.
- [48] Y. Kumar, E. Kibena-Pöldsepp, M. Mooste, J. Kozlova, A. Kikas, J. Aruväli, M. Käärik, V. Kisand, J. Leis, A. Tamm, S. Holdcroft, J. H. Zagal, K. Tammeveski, *ChemElectroChem* **2022**, *9*, e202200717.
- [49] H. Wang, D. J. Liu, *Curr. Opin. Electrochem.* **2021**, *28*, 100724.
- [50] F. Luo, S. Wagner, I. Onishi, S. Selve, S. Li, W. Ju, H. Wang, J. Steinberg, A. Thomas, U. I. Kramm, P. Strasser, *Chem. Sci.* **2021**, *12*, 384.
- [51] N. Levy, L. Elbaz, *Electrocatalysis for Membrane Fuel Cells* **2023**, *6*, <https://doi.org/10.1002/9783527830572.ch6>.
- [52] A. Friedman, L. Landau, S. Gonen, Z. Gross, L. Elbaz, *ACS Catal.* **2018**, *8*, 5024–5031.
- [53] L. Peles-Strahl, N. Zion, O. Lori, N. Levy, G. Bar, A. Dahan, L. Elbaz, *Adv. Funct. Mater.* **2021**, *31*, 2100163.
- [54] A. Friedman, N. R. Samala, H. C. Honig, M. Tasior, D. T. Gryko, L. Elbaz, I. Grinberg, *ChemSusChem* **2021**, *14*, 1886–1892.
- [55] R. Attias, K. V. Sankar, K. Dhaka, W. Moschkowitsch, L. Elbaz, M. C. Toroker, Y. Tsur, *ChemSusChem* **2021**, *14*, 1737–1746.
- [56] W. Zhao, G. Wan, C. Peng, H. Sheng, J. Wen, H. Chen, *ChemSusChem* **2018**, *11*, 3473–3479.
- [57] Y. Luo, J. Zhang, M. Kiani, Y. Chen, J. Chen, G. Wang, S. H. Chan, R. Wang, *Ind. Eng. Chem. Res.* **2018**, *57*, 12087–12095.
- [58] J. N. Liu, B. Q. Li, C. X. Zhao, J. Yu, Q. Zhang, *ChemSusChem* **2020**, *13*, 1529–1536.
- [59] S. Chen, M. Cui, Z. Yin, J. Xiong, L. Mi, Y. Li, *ChemSusChem* **2021**, *14*, 73–93.
- [60] C. Li, H. Zhang, M. Liu, F. F. Lang, J. Pang, X. H. Bu, *Ind. Chem. Mater.* **2023**, *1*, 9–38.
- [61] V. A. Saveleva, K. Kumar, P. Theis, N. S. Salas, U. I. Kramm, F. Jaouen, F. Maillard, P. Glatzel, *ACS Appl. Energy Mater.* **2023**, *6*, 611–616.
- [62] Y. Mun, M. J. Kim, S. A. Park, E. Lee, Y. Ye, S. Lee, Y. T. Kim, S. Kim, O. H. Kim, Y. H. Cho, Y. E. Sung, J. Lee, *Appl. Catal. B: Environ.* **2018**, *222*, 191–199.
- [63] J. Shi, H. Shao, F. Yang, J. Li, L. Fan, W. Cai, *J. Chem. Eng.* **2022**, *445*, 136628.
- [64] X. Xu, C. Xu, J. Liu, R. Jin, X. Luo, C. Shu, H. Chen, C. Guo, L. Xu, Y. Si, *J. Alloys Compd.* **2023**, *939*, 168782.
- [65] S. H. Lee, J. Kim, D. Y. Chung, J. M. Yoo, H. S. Lee, M. J. Kim, B. S. Mun, S. G. Kwon, Y. E. Sung, T. Hyeon, *J. Am. Chem. Soc.* **2019**, *141*, 2035–2045.
- [66] A. Serov, M. H. Robson, M. Smolnik, P. Atanassov, *Electrochim. Acta* **2013**, *109*, 433–439.
- [67] A. Serov, K. Artyushkova, N. I. Andersen, S. Stariha, P. Atanassov, *Electrochim. Acta* **2015**, *179*, 154–160.
- [68] L. Delafontaine, A. Cosenza, E. Murphy, Y. Liu, J. Chen, B. Sun, P. Atanassov, *ACS Appl. Energy Mater.* **2023**, *6*, 678–691.
- [69] H. Adabi, A. Shakouri, N. Ul Hassan, J. R. Varcoe, B. Zulevi, A. Serov, J. R. Regalbuto, W. E. Mustain, *Energy* **2021**, *6*, 834–843.
- [70] A. Serov, K. Artyushkova, P. Atanassov, *Adv. Energy Mater.* **2014**, *4*, 1301735.
- [71] U. Tylus, Q. Jia, K. Strickland, N. Ramaswamy, A. Serov, P. Atanassov, S. Mukerjee, *J. Phys. Chem. C* **2014**, *118*, 8999–9008.
- [72] C. Santoro, A. Serov, R. Gokhale, S. Rojas-Carbonell, L. Stariha, J. Gordon, K. Artyushkova, P. Atanassov, *Appl. Catal. B: Environ.* **2017**, *205*, 24–33.
- [73] A. Serov, M. H. Robson, K. Artyushkova, P. Atanassov, *Appl. Catal. B: Environ.* **2012**, *127*, 300–306.
- [74] M. Mazzucato, C. Durante, *Electrochim. Acta* **2021**, *394*, 139105.
- [75] S. Rojas-Carbonell, K. Artyushkova, A. Serov, C. Santoro, I. Matanovic, P. Atanassov, *ACS Catal.* **2018**, *8*, 3041–3053.
- [76] Y. Huang, Y. Chen, M. Xu, T. Asset, P. Tieu, A. Gili, D. Kulkarni, V. De Andrade, F. De Carlo, H. S. Barnard, A. Doran, D. Y. Parkinson, X. Pan, P. Atanassov, I. V. Zenyuk, *Mater. Today* **2021**, *47*, 53–68.
- [77] Y. Chen, Y. Huang, M. Xu, T. Asset, X. Yan, K. Artyushkova, M. Kodali, E. Murphy, A. Ly, X. Pan, I. V. Zenyuk, P. Atanassov, *Mater. Today* **2022**, *53*, 58–70.
- [78] C. Lo Vecchio, A. Serov, H. Romero, A. Lubers, B. Zulevi, A. S. Aricò, V. Baglio, *J. Power Sources* **2019**, *437*, 226948.
- [79] M. Malagodi, C. Canevari, L. Bonizzoni, A. Galli, F. Maspero, M. Martini, *Appl. Phys. A* **2013**, *112*, 225–234.

- [80] H. C. Honig, S. Mostoni, Y. Presman, R. Z. Snitkoff-Sol, P. Valagussa, M. D'Arienzo, R. Scotti, C. Santoro, M. Muhyuddin, L. Elbaz, *Nanoscale* **2024**, *16*, 11174–11186.
- [81] A. Gentile, S. Marchionna, M. Balordi, G. Pagot, C. Ferrara, V. Di Noto, R. Ruffo, *ChemElectroChem* **2022**, *9*, e202200891.
- [82] C. Strel, P. Kregsamer, P. Wobrauschek, H. Gatterbauer, P. Pianetta, S. Pahlke, L. Fabry, L. Palmethofer, M. Schmeling, *Spectrochim. Acta, Part B* **1999**, *54*, 1433–1441.
- [83] S. Mostoni, M. D'Arienzo, B. Di Credico, L. Armelao, M. Rancan, S. Dirè, E. Callone, R. Donetti, A. Susanna, R. Scotti, *Ind. Eng. Chem. Res.* **2021**, *60*, 10180–10192.
- [84] S. Verhaverbeke, I. Teerlinck, C. Vinckier, G. Stevens, R. Cartuyvels, M. M. Heyns, *J. Electrochem. Soc.* **1994**, *141*, 2852.
- [85] J. S. Judge, *J. Electrochem. Soc.* **1971**, *118*, 1772.
- [86] P. Mctigue, T. A. Odonnell, B. Verity, *Aust. J. Chem.* **1985**, *38*, 1797–1807.
- [87] H. N. Farrer, F. J. C. Rossotti, *J. Inorg. Nucl. Chem.* **1964**, *26*, 1959–1965.
- [88] B. Kim, W. Lee, S. Lim, *Appl. Surf. Sci.* **2024**, *657*, 159829.
- [89] A. Cosenza, L. Delafontaine, A. Ly, H. Wang, E. Murphy, Y. Liu, S. Specchia, P. Atanassov, *J. Power Sources* **2023**, *556*, 232382.
- [90] M. M. Hossen, K. Artyushkova, P. Atanassov, A. Serov, *J. Power Sources* **2018**, *375*, 214–221.
- [91] R. Gokhale, Y. Chen, A. Serov, K. Artyushkova, P. Atanassov, *Electrochem. Commun.* **2016**, *72*, 140–143.
- [92] S. Kabir, K. Artyushkova, A. Serov, B. Kiefer, P. Atanassov, *Surf. Interface Anal.* **2016**, *48*, 293–300.
- [93] M. Huang, R. Ding, J. Yang, W. Shi, S. Shi, L. Chen, S. Liu, X. Yin, *J. Electrochem. Soc.* **2022**, *169*, 106507.
- [94] V. C. A. Ficca, C. Santoro, E. Placidi, F. Arciprete, A. Serov, P. Atanassov, B. Mecheri, *ACS Catal.* **2023**, *13*, 2162–2175.
- [95] A. Zitolo, V. Goellner, V. Armel, M. T. Sougrati, T. Mineva, L. Stievano, E. Fonda, F. Jaouen, *Nature Mater.* **2015**, *14*, 937–942.
- [96] J. Li, M. T. Sougrati, A. Zitolo, J. M. Ablett, I. C. Oğuz, T. Mineva, I. Matanovic, P. Atanassov, Y. Huang, I. Zenyuk, A. Di Cicco, K. Kumar, L. Dubau, F. Maillard, G. Dražić, F. Jaouen, *Nature Catal.* **2021**, *4*, 10–19.
- [97] S. Kabir, K. Artyushkova, A. Serov, P. Atanassov, *ACS Appl. Mater. Interfaces* **2018**, *10*(14), 11623–11632.
- [98] H. An, K. Min, Y. Lee, R. Na, S. E. Shim, S. H. Baeck, *Mol. Catal.* **2022**, *530*, 112589.
- [99] W. Zhang, T. Cui, L. Yang, C. Zhang, M. Cai, S. Sun, Y. Yao, X. Zhuang, F. Zhang, *J. Colloid. Interf. Sci.* **2017**, *497*, 108–116.
- [100] V. Duraisamy, K. Selvakumar, R. Krishnan, S. M. Senthil Kumar, *ChemistrySelect* **2019**, *4*, 2463–2474.
- [101] H. Chen, Q. H. Li, W. Yan, Z. G. Gu, J. Zhang, *Chem. Eng. J.* **2020**, *401*, 126149.
- [102] T. Wu, Y. Wang, H. Zhao, J. Dong, J. Xu, *J. Colloid. Interf. Sci.* **2021**, *603*, 706–715.
- [103] Z. Yan, C. Dai, X. Lv, M. Zhang, X. Zhao, J. Xie, *J. Alloys Compd.* **2019**, *773*, 819–827.
- [104] L. Fan, L. Zhang, X. Li, H. Mei, M. Li, Z. Liu, Z. Kang, Y. Tuo, R. Wang, D. Sun, *Inorg. Chem. Front.* **2022**, *9*, 4101–4110.
- [105] M. Muhyuddin, N. Zocche, R. Lorenzi, C. Ferrara, F. Poli, F. Soavi, C. Santoro, *Mater. Renew. Sustain. Energy* **2022**, *11*, 131–141.
- [106] Y. Xie, X. Yu, Z. Jin, Q. Liu, S. Liu, Y. Zhao, Z. Xiang, *ASEM* **2022**, *1*, 100006.
- [107] V. Duraisamy, S. Venkateshwaran, R. Thangamuthu, S. M. Senthil Kumar, *Int. J. Hydrogen Energy* **2022**, *47*, 40327–40339.
- [108] F. Sun, T. Liu, M. Huang, L. Guan, *Sustain. Energ. Fuels* **2023**, *7*, 3675–3683.
- [109] J. Y. Cheon, T. Kim, Y. Choi, H. Y. Jeong, M. G. Kim, Y. J. Sa, J. Kim, Z. Lee, T. H. Yang, K. Kwon, O. Terasaki, G. G. Park, R. R. Adzic, S. H. Joo, *Sci. Rep.* **2013**, *3*, 2715.
- [110] W. Stöber, A. Fink, E. Bohn, *J. Colloid. Interf. Sci.* **1968**, *26*, 62–69.
- [111] L. Mezzomo, S. Bonato, S. Mostoni, B. Di Credico, R. Scotti, M. D'Arienzo, P. Mustarelli, R. Ruffo, *Electrochim. Acta* **2022**, *411*, 140060.
- [112] D. M. Knotter, *J. Am. Chem. Soc.* **2000**, *122*, 4345–4351.

Manuscript received: June 3, 2024

Revised manuscript received: September 10, 2024

Accepted manuscript online: September 26, 2024

Version of record online: November 7, 2024